SI Appendix

Lability of Secondary Organic Particulate Matter

Pengfei Liu[a], Yong Jie Li[a,b], Yan Wang[a,c], Mary K. Gilles[d], Rahul A. Zaveri[e], Allan K. Bertram[f], and Scot T. Martin[a,g,1]

[a]John A. Paulson School of Engineering and Applied Sciences, Harvard University, Cambridge, MA 02138;

[b]Department of Civil and Environmental Engineering, Faculty of Science and Technology, University of Macau, Macau, China;

[c]T. H. Chan School of Public Health, Harvard University, Boston, MA 02115;

[d]Chemical Sciences Division, Lawrence Berkeley National Laboratory, Berkeley, CA 94720;

[e]Atmospheric Sciences and Global Change Division, Pacific Northwest National Laboratory, Richland, WA 99354;

[f]Department of Chemistry, University of British Columbia, Vancouver, BC VT6 1Z1, Canada;

[g]Department of Earth and Planetary Sciences, Harvard University, Cambridge, MA 02138

E-mail: scot_martin@harvard.edu

Proceedings of the National Academy of Science of the United States of America

[1]To Whom Correspondence Should be Addressed

S1. Film Preparation

Different types of secondary organic material were produced in aerosol form by the reactions of precursor gaseous compounds in an oxidation flow reactor (OFR) (1, 2), as described previously (3). α-Pinene was oxidized by ozone in the dark. Isoprene, toluene, and *m*-xylene were primarily oxidized by hydroxyl (OH) radicals, which were produced by photochemical reactions of ozone and water vapor under ultraviolet illumination (254 nm). Reaction conditions were 293 ± 2 K and 15 ± 3% RH. The aerosol particle populations were characterized by a Scanning Mobility Particle Sizer (SMPS; TSI Inc.) (4) and an Aerosol Mass Spectrometer (HR-ToF-AMS; Aerodyne Research Inc.) (5). Experimental conditions, mass concentrations, and elemental ratios for the different types of SOM are listed in Table S4. Organic films were grown by passing the various aerosol particle populations exiting the OFR into an electrostatic precipitator (TSI 3089). A QCM quartz crystal was mounted inside the precipitator (6). By particle deposition, a uniform organic film grew and coated the crystal surface. A continuous thin film morphology (rather than single particles) was confirmed previously using atomic force microscopy and optical microscopy (6). Film thickness and mass ranged from 30 to 200 nm and 4 to 20 μg, respectively (Table S4). The maximum mass contributed by absorbed water is estimated as 20% of the film mass at the highest RH values of this study, and a correction is included in the reported vapor mass concentrations.

S2. Vapor Mass Concentrations

After film preparation, the quartz crystal was removed from the precipitator and sealed in a covered Petri dish using Teflon tape. Within 10 min, the sample was mounted into a flow cell of a Quartz-Crystal Microbalance (Biolin Scientific Q-sense QSX 303 and Q-sense E4). The schematic diagram for the QCM apparatus is illustrated in Fig. S1. The operating principle is that

changes Δf in the resonant frequency of the quartz crystal, are proportional by a sensitivity factor ζ to changes Δm in mass of material on the sensor. The equation is written as $\Delta m = -\zeta \Delta f$.

The cell allowed an RH-regulated nitrogen gas flow to pass across the surface of the film. A flow Q of 6 to 8 $cm^3\ min^{-1}$ was used from <1% to 60% RH at 293.15 ± 0.1 K, resulting in a plug-flow-equivalent residence time of 0.3 to 0.4 s in the cell. By comparison, SVOC molecules evaporating from the film diffused across the cell headspace within 0.05 s. These time scales did not depend on the mass accommodation coefficient, or the surface area of the sample (cf. Table S5). The headspace of the flow cell became saturated and reached local equilibrium with respect to the composition of the surface region of the film.

The vapor mass concentration C in the flow exiting the QCM was related to the mass lost from the organic film during a time interval Δt, as follows: $C = \left|\Delta m \left(Q\ \Delta t\right)^{-1}\right|$. For fixed C and Δt, the mass loss was proportional to the flow rate. In a control experiment, this relation was confirmed for a flow rate from 1 to 15 $cm^3\ min^{-1}$ of *n*-octadecane (Fig. S4). This experiment also verified that the obtained C of (2.1 ± 0.2) × 10^3 µg m^{-3} was within the uncertainty of the literature value of (1.4 to 2.0) × 10^3 µg m^{-3} for the equilibrium vapor mass concentration of *n*-octadecane (7, 8). For ζ = 17.7 ng $cm^{-2}\ Hz^{-1}$ (provided by crystal vendor), mass changes on the order of 1 ng could be detected. This mass change corresponded to a vapor mass concentration of 0.1 µg m^{-3} or above for the employed experiment conditions of Q and Δt.

S3. Infrared spectroscopy.

In a complementary set of experiments, infrared spectra were recorded during evaporation using an attenuated total reflectance (ATR) accessory (Pike Technologies) in a Fourier transform infrared spectrometer (FTIR, Nicolet 670). For spectroscopic characterization, particles were first collected onto a Teflon filter, which was then pressed onto the surface of a

germanium crystal (9). The SOM-laden germanium element was housed within the ATR accessory, which served as a flow cell. The cell was continuously purged by 20 cm^3 min^{-1} of RH-regulated nitrogen. Infrared spectra were recorded at 3-min intervals. The initial spectra of different types of SOM at <5% RH are shown in Fig. S5. From the spectra, absorption bands of functional groups were identified and integrated for area (3).

For the RH dependence of *C* observed for toluene-derived SOM (cf. main text), an alternative explanation can be that the oligomers in the SOM were hydrolyzed at elevated RH. Consequently the intrinsic volatility decreased. This hypothesis was tested using infrared spectroscopy. For toluene-derived SOM thin films, changes of organic functional groups during evaporation were observed at different RHs (Fig. S6). The results indicate that the RH-dependent mass loss rates measured by the QCM were mostly explained by the evaporation of carbonyl groups (C=O) (Fig. S6a). The RH dependence was less pronounced for other functional groups, such as ether (C−O), alcoholic and phenolic hydroxyl (O−H), and carboxylic hydroxyl (carboxylic O−H) (Fig. S6 b to d). Given a similar carbon number, organic compounds with carbonyl groups, such as aldehydes and ketones, were typically more volatile than other oxygenated compounds (10). For the suggestion that the volatile carbonyl compounds were produced from hydrolysis of non-carbonyl compounds, an increase in the C=O band in the infrared spectra after hydration would be expected. However, the C=O band decreased with increasing RH (Fig. S7). Alternatively, if the volatile carbonyl compounds were converted from the less-volatile carbonyl compounds, a significant shift of the position of C=O peak would be expected. This shift, however, was not observed. As the RH increased from < 5% to 54%, a small blue shift of peak position from 1730 to 1735 cm^{-1} were observed (inset of Fig. S7). This small shift in peak position was consistent with an effect of hydrogen bonding associated with

the hydration (9, 11). The nature of the carbonyl, however, was not significantly changed. In sum, no evidence of chemical decomposition was found from the infrared datasets.

S4. Kinetic Modeling

A slab model to numerically simulate diffusion was developed to retrieve an effective self-diffusivity D_{org} of organic species. The primary data constraint was the relationship between vapor mass concentrations and remaining mass fractions for the different types of films (main text, Fig. 2). Gas, surface, and interior concentrations were dynamically updated according to the gas flow rate and assuming local equilibrium at the gas-surface interface. The model treatment assumed that diffusivity did not change as local composition was altered by mass transport and evaporation. Volatility changes during evaporation due to changes in the composition of the surface region were modeled by assuming that Raoult's law for an ideal solution was obeyed. Particle diameters and mean free path in the gas phase corresponded to the transition regime (i.e., Knudsen number between 0.1 and 10). As described in the main text, two models were compared (Models 1 and 2) to describe composition. The model was developed for geometries corresponding both to an infinite horizontal slab, which was used for the film data sets, as well as for a sphere, which was used to model implications for atmospheric particles. For the latter, the characteristic time for evaporation in scenarios for atmospheric particles were calculated based on the retrieved D_{org} values (main text, Fig. 3). Further details of the model are presented below.

S4.1 Model framework

The model framework is developed based on both the thermodynamic and the kinetic considerations. The secondary organic material (SOM) is a mixture of different organic species. The vapor mass concentrations of these species in pure form span many orders of magnitude. Thermodynamically, these species can be modeled as a set of N lumped volatile components, X_1,

X_2, ..., X_N. The overall vapor mass concentration C over the surface region of the SOM can be expressed as:

$$C = \sum_{i=1}^{n} x_i f_i C_i^0 \quad \text{(S1)}$$

The term x_i denotes the mole fraction of component i in the SOM surface region at the film-vapor interface. In the simulation, different components are assumed to have the same effective molecular weight of 0.15 kg mol^{-1}, following Riipinen et al. (12) and Vaden et al. (13) In this case, x_i also denotes the mass fraction of component i. The value of effective molecular weight can vary among different chemical systems. The simulation results, however, are largely insensitive to the absolute value of the molecular weight. The term f_i is the activity coefficient. An ideal solution assumption is used herein (f_i = 1). The term C_i^0 is the vapor mass concentration of component i in pure form.

Kinetically, the model explicitly simulates the species diffusion of different components using a multi-slab framework. The shrinkage or growth of the system because of evaporation or condensation is considered in modeling. Herein, a nonvolatile component X_0 is introduced as a reference compound, and the coordinate system is constructed based on the mass of X_0 (14, 15). This treatment avoids the complication of a moving boundary problem for conventional space coordinate systems because the mass of nonvolatile reference component does not change with time. By defining a geometry factor v, a universal diffusion equation is derived. It can be used for a slab (thin film; v = 0), a cylinder (v = 1), or a sphere (particle; v = 2), as follows (14):

$$\frac{\partial u_i}{\partial \tau} = \frac{\partial}{\partial \phi}\left(D_r Z^2(\nu) \frac{\partial u_i}{\partial \phi} \right) \quad \text{(S2)}$$

where u_i is defined as the ratio of the mass concentration of the migrating component c_i (kg m^{-3}) to that of the reference compound c_0 (kg m^{-3}):

$$u_i = c_i / c_0 = x_i / x_0 \tag{S3}$$

τ is the dimensionless time, which is defined as:

$$\tau = \frac{D_0 c_0^2(0)}{\rho_0^2 L_0^2} t \tag{S4}$$

for the initial mass concentration $c_0(0)$ of the nonvolatile reference component (kg m^{-3}), the reference diffusivity D_0 (m^2 s^{-1}) (can be any value), and the material density ρ_0 (kg m^{-3}) for the reference component. For a supported thin film, L_0 is the thickness of the film consisting only the reference component. For a spherical particle, $L_0 = d_0 / 2$, where d_0 is the diameter of the particle consisting only of the reference component. L_0 does not change with time. L_0 is related to the initial film thickness $L(0)$ by:

$$L_0 = \left(\frac{c_0(0)}{\rho_0} \right)^{1/(\nu+1)} L(0) \tag{S5}$$

The dimensionless space coordinate ϕ is defined as:

$$\phi = \frac{\int_0^l c_0(t) l^\nu \mathrm{d}l}{\int_0^L c_0(t) l^\nu \mathrm{d}l} = \frac{\nu+1}{c_0(0) L_0^{\nu+1}} \int_0^l c_0(t) l^\nu \mathrm{d}l \tag{S6}$$

where L is the thickness of the film. For a spherical particle, L is the particle radius ($L = d / 2$). The value of ϕ ranges from 0 to 1. The dimensionless diffusivity D_r is defined as:

$$D_r = \frac{D_{\mathrm{org}} c_0^2(t)}{D_0 c_0^2(0)} \tag{S7}$$

The dimensionless geometry variable $Z(\nu)$ is defined as:

$$Z(\nu) = (\nu+1) \left\{ \int_0^\phi \left(1 + \sum_{i=1}^{N} \frac{\rho_0}{\rho_i} u_i \right) \mathrm{d}\phi \right\}^{\frac{\nu}{1+\nu}} \tag{S8}$$

Finally, for an assumption that the volumes of water and solute are additive, the mass concentration c_0 can be related to u, as follows:

$$c_0 = \left(\frac{1}{\rho_0} + \sum_{i=1}^{N} \frac{u_i}{\rho_i} \right)^{-1} \quad \text{(S9)}$$

The equations S8 and S9 can be further simplified by using the same material density for all components ($\rho_i = \rho_0$, for i = 1, 2, ..., N). The material density value is calculated from the HR-ToF-AMS measured elemental ratios for each SOM using the equation in Kuwata et al. (16) (cf. Table S4). The initial film thickness is calculated using the material density and the mass measured by the QCM (cf. Table S4).

S4.2 Evaporation of SOM thin films in the gas-saturation flow cell (v = 0)

Evaporation of SOM thin films in the QCM flow cell is simulated using the model framework described above for the geometry configuration of a slab (cf. Fig. 2 and Fig. S2). The simulation assumes saturation of the nitrogen carrier gas by evaporating substances from the surface layer of the thin film. To test this assumption, an analysis of characteristic time scales is performed and presented in Table S5. The analysis indicates that the plug-flow-equivalent residence time τ_{res} of the carrier gas is significantly longer than the characteristic time required to reach gas saturation. The characteristic time for gas saturation, determined by the mass accommodation of gas molecules at the gas-surface interface and diffusion and mixing in the cell headspace, is independent of the saturation vapor mass concentration C^0 of the volatile component. For a component of low C^0, the mass flux between the surface and gas can be low because it is proportional to C^0. However, the absolute amount of molecules required for saturation in the cell headspace is also low. For this reason, the gas-saturation time scale can still be very short given the geometry and flow rate of the apparatus for this study. This gas-saturation assumption was confirmed by experiments for a pure compound. The experiment

shows that the mass loss is proportional to the flow rate and a constant value of vapor mass concentration is obtained at different flow rates (Fig. S4). The timescale analysis also confirms that particle-phase diffusion can be slower than the residence time for a sufficiently low diffusivity (Table S5), indicating that the diffusivity can be retrieved for these conditions (cf. S4.3).

Initial and boundary conditions are needed to solve the generalized diffusion equation. The initial components are assumed to be well mixed. For evaporation of SOM thin films in the QCM flow cell within gas saturation regime, the initial and boundary conditions are as follows.

$$u_i(0) = x_i(0) / x_0(0) \tag{S10}$$

$$\frac{D_0 c_0^2(0)}{\rho_0 L_0}\left(D_r Z(\nu)\frac{\partial u_i}{\partial \phi}\right)\Bigg|_{\phi=1} = -\frac{Q}{S}\frac{u_i(\phi=1)}{1+\sum_{i=1}^{N} u_i(\phi=1)} C_i^0 \tag{S11}$$

$$\left(D_r Z(\nu)\frac{\partial u_i}{\partial \phi}\right)\Bigg|_{\phi=0} = 0 \tag{S12}$$

Q is the flow rate and $S = 7.85\times10^{-5}$ m^2 is the area of the QCM sensor. The partial differential equation (Eq. S2) is numerically solved by an algorithm implemented in MATLAB.

S4.3 Retrieval of D_{org} from the evaporation of thin films

Evaporation of SOM thin films is simulated using the kinetic model described above with two different volatility schemes (cf. main text). The first scheme (Model 1) assumes that SOM consists of (i) a volatile fraction having a mass vapor concentration C_1^0 and an initial mass fraction of $x_1(0)$ and (ii) a nonvolatile reference component having an initial mass fraction of $x_0(0) = 1\text{-}x_1(0)$. This volatile/nonvolatile model has three free parameters, $u(0) = x_1(0) / [1\text{-}x_1(0)]$, C^0, and D_{org}. For a set of parameters, the evolution of the mass of the thin film can be simulated. An alternative model assumed a mixture consisting of a non-volatility fraction and four volatile

fractions with decadal volatility bins. Herein, the free parameters are the mass fractions $x_i(0)$ (i = 1, 2, 3, and 4) for these volatility bins. Except for D_{org}, parameters are obtained based on the datasets of C observed above the threshold RH (Table S1). D_{org} values are simultaneously optimized. Because these observations are dominated by thermodynamic factors, the D_{org} values cannot be accurately determined, and lower limit values are reported (Table S2). In contrast, the obtained volatility parameters do not strongly depend on D_{org} and thus are robust. These volatility parameters are held constant for datasets below the threshold RH (e.g., toluene-derived material at <1% and 33% RH), and D_{org} values are optimized. The D_{org} values obtained in this region are well constrained, and the uncertainties are within a factor of 2 (Table S2).

S4.4 Evaporation of SOM particles in the infinite, clean air (ν = 2)

The kinetic model is also used for modeling evaporation of spherical particles. Herein L in diffusion equations (cf. S4.1) represent the radius of the particle: $L = d / 2$ where d is the diameter of the particle. The mass flow (kg s^{-1}) for component i is given by (17):

$$J_i = -2\pi d D_g F_{FS} \left(\frac{u_i(\phi = 1)}{1 + \sum_{i=1}^{N} u_i(\phi = 1)} C_i^0 F_K - C_\infty \right) \quad \text{(S13)}$$

where $D_g = 5\times10^{-6}$ m^2 s^{-1} is the gas-phase diffusivity (12, 13), and $C_\infty = 0$ is the gas-phase concentration of volatile component infinitely far from the particle. F_K is the correction term for Kelvin effect:

$$F_K = \exp\left(\frac{4\sigma M}{RTd\rho} \right) \quad \text{(S14)}$$

A surface tension value of σ = 0.05 N m^{-1} is used for calculating F_K (12, 13). ρ is the material density of the particle. F_{FS} is the Fuchs-Sutugin correction for noncontinuum effect and imperfect mass accommodation, given as follows:

$$F_{FS} = \frac{0.75\alpha(1+\mathrm{Kn})}{\mathrm{Kn}^2 + \mathrm{Kn} + 0.283\alpha\mathrm{Kn} + 0.75\alpha} \tag{S15}$$

where α is the mass accommodation coefficient and Kn is the Knudsen number, defined as:

$$\mathrm{Kn} = \frac{2\lambda}{d} \tag{S16}$$

and λ is the mean free path.

For evaporation of a SOM particle, the initial and boundary conditions are given as follows.

$$u_i(0) = x_i(0) / x_0(0) \tag{S17}$$

$$\frac{D_0 c_0^2(0)}{\rho_0 L_0}\left(D_r Z(\nu)\frac{\partial u_i}{\partial \phi}\right)\Bigg|_{\phi=1} = \frac{J_i}{\pi d^2} \tag{S18}$$

$$\left(D_r Z(\nu)\frac{\partial u_i}{\partial \phi}\right)\Bigg|_{\phi=0} = 0 \tag{S19}$$

S4.5 Diffusivity-limited and volatility-limited kinetic regimes

Without kinetic limitation of D_{org}, an intrinsic evaporation time scale can be calculated as:

$$\tau_{\mathrm{is}} = -\frac{m_i(0)}{J_i(0)} = \frac{\rho d^2}{12 D_g F_{FS} F_K C_i^0} \tag{S20}$$

where $m_i(0)$ is the initial mass of volatile component, and $J_i(0)$ is the initial mass flow of volatile component.

The characteristic timescale of in-particle diffusion is given by (17):

$$\tau_{\mathrm{mix}} = \frac{d^2}{4\pi^2 D_{\mathrm{org}}} \tag{S21}$$

The diffusivity-limited kinetic regime is defined as $\tau_{\mathrm{mix}} > \tau_{\mathrm{is}}$, and an otherwise condition is the volatility-limited regime. For a critical value $\tau_{\mathrm{mix}} = \tau_{\mathrm{is}}$, the boundary between the two kinetic regimes is defined as follows (18):

$$\xi^{*} = \frac{D_{\mathrm{org}}}{C_i^0} = \frac{3D_g F_{FS} F_K}{\pi^2 \rho} \tag{S22}$$

The specific ξ^{*} value is plotted in Fig. S4 for a range of particle diameters *d* and mass accommodation coefficients α.

Supplementary References

1. Kang E, Root MJ, Toohey DW, & Brune WH (2007) Introducing the concept of Potential Aerosol Mass (PAM). *Atmos. Chem. Phys.* 7(22):5727-5744.
2. Lambe AT, *et al.* (2011) Characterization of aerosol photooxidation flow reactors: heterogeneous oxidation, secondary organic aerosol formation and cloud condensation nuclei activity measurements. *Atmos. Meas. Tech.* 4(3):445-461.
3. Liu PF, *et al.* (2015) Ultraviolet and visible complex refractive indices of secondary organic material produced by photooxidation of the aromatic compounds toluene and m-xylene. *Atmos. Chem. Phys.* 15(3):1435-1446.
4. Wang SC & Flagan RC (1990) Scanning electrical mobility spectrometer. *Aerosol Sci. Technol.* 13(2):230-240.
5. DeCarlo PF, *et al.* (2006) Field-deployable, high-resolution, time-of-flight aerosol mass spectrometer. *Anal. Chem.* 78(24):8281-8289.
6. Liu P, Zhang Y, & Martin ST (2013) Complex refractive indices of thin films of secondary organic materials by spectroscopic ellipsometry from 220 to 1200 nm. *Environ. Sci. Technol.* 47(23):13594-13601.
7. Fonseca JMS, Gushterov N, & Dohrn R (2014) Vapour pressures of selected organic compounds down to 1 mPa, using mass-loss Knudsen effusion method. *J. Chem. Thermodyn.* 73(0):148-155.
8. Bradley RS & Shellard AD (1949) *The Rate of Evaporation of Droplets. III. Vapour Pressures and Rates of Evaporation of Straight-Chain Paraffin Hydrocarbons* pp 239-251.
9. Hung H-M, Chen Y-Q, & Martin ST (2013) Reactive aging of films of secondary organic material studied by infrared spectroscopy. *J. Phys. Chem. A* 117(1):108-116.
10. Capouet M & Müller JF (2006) A group contribution method for estimating the vapour pressures of α-pinene oxidation products. *Atmos. Chem. Phys.* 6(6):1455-1467.
11. Fried SD, Bagchi S, & Boxer SG (2013) Measuring Electrostatic Fields in Both Hydrogen-Bonding and Non-Hydrogen-Bonding Environments Using Carbonyl Vibrational Probes. *J. Am. Chem. Soc.* 135(30):11181-11192.
12. Riipinen I, Pierce JR, Donahue NM, & Pandis SN (2010) Equilibration time scales of organic aerosol inside thermodenuders: Evaporation kinetics versus thermodynamics. *Atmos. Environ.* 44(5):597-607.
13. Vaden TD, Imre D, Beránek J, Shrivastava M, & Zelenyuk A (2011) Evaporation kinetics and phase of laboratory and ambient secondary organic aerosol. *Proc. Natl. Acad. Sci. U.S.A.* 108(6):2190-2195.
14. Liou JK & Bruin S (1982) An approximate method for the nonlinear diffusion problem with a power relation between diffusion coefficient and concentration—I. Computation of desorption times. *Intl. J. Heat Mass Transfer* 25(8):1209-1220.
15. Yamamoto S, Coumans W, & Vlugt T (1997) Determining concentration dependent diffusivity in food materials. *Eng. Food* 1:A164-A167.
16. Kuwata M, Zorn SR, & Martin ST (2012) Using elemental ratios to predict the density of organic material composed of carbon, hydrogen, and oxygen. *Environ. Sci. Technol.* 46(2):787-794.
17. Seinfeld JH & Pandis SN (2006) *Atmospheric Chemistry and Physics: From Air Pollution to Climate Change* (John Wiley & Sons).

18. Riipinen I, *et al.* (2012) The contribution of organics to atmospheric nanoparticle growth. *Nature Geosci* 5(7):453-458.
19. Chen Q, Liu Y, Donahue NM, Shilling JE, & Martin ST (2011) Particle-phase chemistry of secondary organic material: modeled compared to measured O:C and H:C elemental ratios provide constraints. *Environ. Sci. Technol.* 45(11):4763-4770.

SOM type	Parameter	Nonvolatile/ volatile components	Five-component decadal volatility basis set
Toluene + OH (M_{org} = 90 μg m^{-3})	C_i^0	**0**, *2800*	**0**, **10**, **100**, **1000**, **10000**
	$x_i(0)$	*0.862*, *0.138*	*0.653*, *0.130*, *0.070*, *0.090*, *0.057*
	D_{org}	depends on RH	depends on RH
Isoprene + OH (M_{org} = 90 μg m^{-3})	C_i^0	**0**, *8500*	**0**, **10**, **100**, **1000**, **10000**
	$x_i(0)$	*0.667*, *0.333*	*0.124*, *0.247*, *0.124*, *0.247*, *0.259*
	D_{org}	depends on RH	depends on RH
α-Pinene + O_3 (M_{org} = 140 μg m^{-3})	C_i^0	**0**, *4000*	**0**, **10**, **100**, **1000**, **10000**
	$x_i(0)$	*0.833*, *0.167*	*0.214*, *0.310*, *0.227*, *0.192*, *0.058*
	D_{org}	depends on RH	depends on RH

Table S1. Volatility distributions derived from evaporation of SOM thin films, as represented by volatility bins C_i^0 (μg m^{-3}) and initial mole fractions $x_i(0)$ of each component *i*. Bold shows a priori quantities. Italics shows quantities retrieved from the model based on constraints to the collected data sets. All terms in this table, except D_{org}, are taken as independent of relative humidity. They are derived for data sets at high relative humidity that are not kinetically limited. At lower RH values, D_{org} is the optimized quantity while other quantities are held constant (Table S2).

SOM type	Relative humidity	Retrieved D_{org} (m^2 s^{-1})	
		Model 1	Model 2
Toluene + OH	<5%	$3^{+2}_{-1} \times 10^{-22}$	$1^{+1}_{-0.5} \times 10^{-22}$
Toluene + OH	33%	$3^{+2}_{-1} \times 10^{-21}$	$2^{+2}_{-1} \times 10^{-21}$
Toluene + OH	54%	$> 1^{+9}_{-0.6} \times 10^{-19}$ *	$> 2^{+8}_{-1} \times 10^{-19}$
Isoprene + OH	<5%	$> 1^{+9}_{-0.5} \times 10^{-18}$	$> 1^{+9}_{-0.5} \times 10^{-18}$
α-Pinene + O_3	<5%	$> 1^{+9}_{-0.5} \times 10^{-18}$	$> 1^{+9}_{-0.7} \times 10^{-18}$

Table S2. Retrieved effective diffusivities Dorg for different types of organic films. Models 1 and 2 are described in the main text. *Lower limits to diffusivity were obtained when the observed vapor mass concentrations were not kinetically limited.

SOM type	Parameter	Value	Description	M_{org} range (µg m^{-3})	Reference
Toluene + OH (M_{org} = 90 µg m^{-3})	C_i^0	1, 10, 100, 1000	Decadal volatility derived from particle mass yield of toluene photooxidation at 293 K, < 20% RH, and low NO_x.	3 to 100	Hildebrandt et al., 2008
	α_i	0.01, 0.24, 0.7, 0.7			
	$x_i(0)$	0.016, 0.346, 0.542, 0.096			
α-Pinene + O_3 (M_{org} = 140 µg m^{-3})	C_i^0	0.01, 0.1, 1, 10, 100, 1000, 10000	Decadal volatility derived from particle yield of α-pinene dark ozonolysis at 298 K, < 10% RH, and low NO_x.	0.1 to 400	Pathak et al., 2007
	α_i	0.001, 0.012, 0.037, 0.088, 0.099, 0.250, 0.800			
	$x_i(0)$	0.004, 0.052, 0.159, 0.354, 0.250, 0.133, 0.048			

Table S3. Volatility parameters reported in literature, as presented by volatility bins C_i^0 (µg m^{-3}) and relative mass yields α_i. The initial mass fractions $x_i(0)$ of the particle composition are calculated and listed for the M_{org} values of this study (listed in the first column). Literature sources are selected for which the ranges of M_{org} overlap with the M_{org} measured in this study. The calculated evaporation rate and vapor concentration are shown in Figs. 2 and S2 as a function of mass fraction of remaining material.

		Aerosol Form					
Precursor	Oxidant	Organic particle mass concentration M_{org} (μg m^{-3})[a]	O:C[b]	H:C[b]	Material density (kg m^{-3})[c]	Initial film mass (μg)	Initial film thickness (nm)
toluene	OH	90 ± 10	1.08	1.69	1.55×10^3	3.8-6.1	31-50
m-xylene	OH	70 ± 20	0.88	1.70	1.45×10^3	17.1	150
α-pinene	O_3	140 ± 30	0.43	1.70	1.19×10^3	19.1	204
isoprene	OH	90 ± 40	0.82	1.90	1.36×10^3	15.3	143

[a] Values derived from number-diameter distributions measured by a Scanning Mobility Particle Sizer (SMPS) and analyzed using the listed material density.

[b] Values derived from analysis of mass spectra recorded by a High-Resolution Time-of-Flight Aerosol Mass Spectrometer (HR-TOF-AMS). Analysis was based on the approach described by Chen et al. (19)

[c] Values calculated from the O:C and H:C ratios using the method of Kuwata et al. (16)

Table S4. Precursor, oxidant, organic particle mass concentrations, elemental ratios, material densities, initial film mass, and film thickness for the different types of SOM studied herein.

Process	Equation	Time scale (s)
Plug-flow equivalent residence time	$\tau_{\mathrm{res}} = VQ^{-1}$	0.3 - 0.4
Equilibration time scale between the surface region of the film and the boundary layer	$\tau_{\mathrm{eq,s}} = l\alpha^{-1}\sqrt{\pi m(8kT)^{-1}}$	$(0.04 - 7) \times 10^{-9}$
Time scale of gas molecules diffuse in the cell head space	$\tau_{\mathrm{dg}} = V^2 A^{-2} D_g^{-1}$	0.05
Time scale of organic molecules diffuse in the thin film	$\tau_{\mathrm{ds}} = L^2 D_{\mathrm{org}}^{-1}$	$9 \times 10^{-7} - 9 \times 10^{8}$

Table S5. Estimated characteristic time scales of different processes related to the mass loss of the thin film in the QCM apparatus.

Coefficient	Symbol	Value	Unit
Volume of the QCM cell	V	4×10^{-8}	m^3
Surface area of the thin film	A	7.85×10^{-5}	m^2
Nitrogen flow rate	Q	$(1.0 - 1.33) \times 10^{-7}$	$m^3\ s^{-1}$
Temperature	T	293.15	K
Thickness of the SOM thin film	L	$3 \times 10^{-8} - 3 \times 10^{-7}$	m
Mass accommodation coefficients	α	0.1 - 1	1
Diffusivity of organic molecules in nitrogen	D_g	5×10^{-6}	$m^2\ s^{-1}$
Diffusivity of organic molecules in the thin film	D_{org}	$10^{-22} - 10^{-9}$	$m^2\ s^{-1}$
Thickness of boundary layer at the gas-surface interface	l	$10^{-7} - 10^{-6}$	m
Mass of the organic molecules	m	$(1.7 - 5.0) \times 10^{-25}$	kg
Boltzmann constant	k	1.38×10^{-23}	$m^2\ kg\ s^{-2}\ K^{-1}$

Table S6. Summary table for coefficients used in the calculation of characteristic time scales listed in Table S5.

List of Supplementary Figures

Figure S1. Schematic diagram of the apparatus for vapor concentration measurement based on the quartz-crystal microbalance (QCM).

Figure S2. As for Fig. 2 but for decadal volatility basis set model considering particle phase diffusion.

Figure S3. The critical value of the diffusivity to volatility ratio (ξ^*) that defines the boundary of two kinetic regimes. Data are shown as a function of particle diameter for different values of mass accommodation coefficient α.

Figure S4. Sublimation pressure of *n*-octadecane measured at 298.15 K for method validation. (a) Evaporation rates measured at different flow rates. (b) Sublimation pressures measured at different flow rates. Literature data are shown for comparison (7, 8). For each data point, error bar shows the one-sigma uncertainty propagated from the QCM measurement. Red shading shows the overall uncertainty of multiple measurements (95% confidence interval). Gray shading represents the estimated gas-saturation regime. The ratio between residence time τ_{res} to characteristic time τ_{dg} of gas diffusion in the flow cell is marked on upper axis.

Figure S5. Infrared spectra for different types of secondary organic material. Spectra were taken at dry condition (RH < 5%). Shading areas show the absorption bands of oxygenated functional groups.

Figure S6. Evaporation of different functional groups for toluene-derived secondary organic material measured by infrared spectroscopy. Data are normalized by the initial band areas. Colors represent data measured at different relative humidities. The determination of band areas is described in Liu et al. (3)

Figure S7. Infrared spectra for toluene-derived secondary organic material measured at different values of relative humidity. Inset shows an expanded view for the carbonyl absorption band in the region of 1550 to 1900 cm^{-1}.

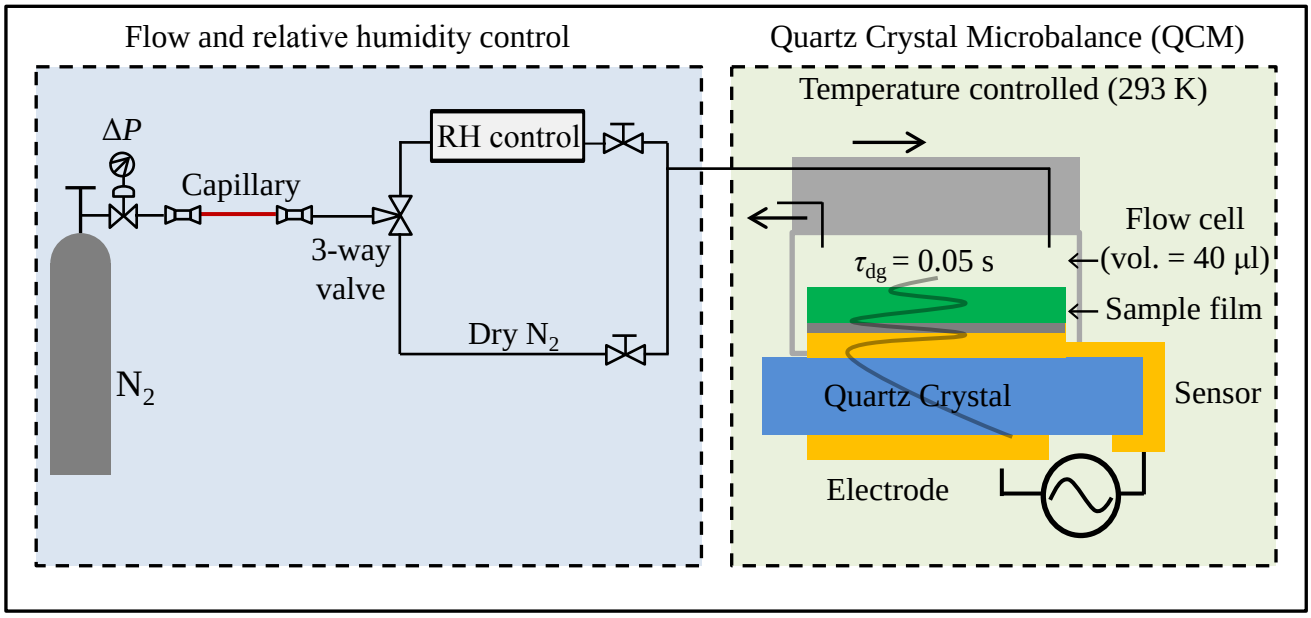
Flow and relative humidity control
Quartz Crystal Microbalance (QCM)
Temperature controlled (293 K)
ΔP
Capillary
RH control
3-way
valve
Dry N2
N2
Flow cell
(vol. = 40 µl)
τdg = 0.05 s
Sample film
Quartz Crystal
Sensor
Electrode

Figure S1

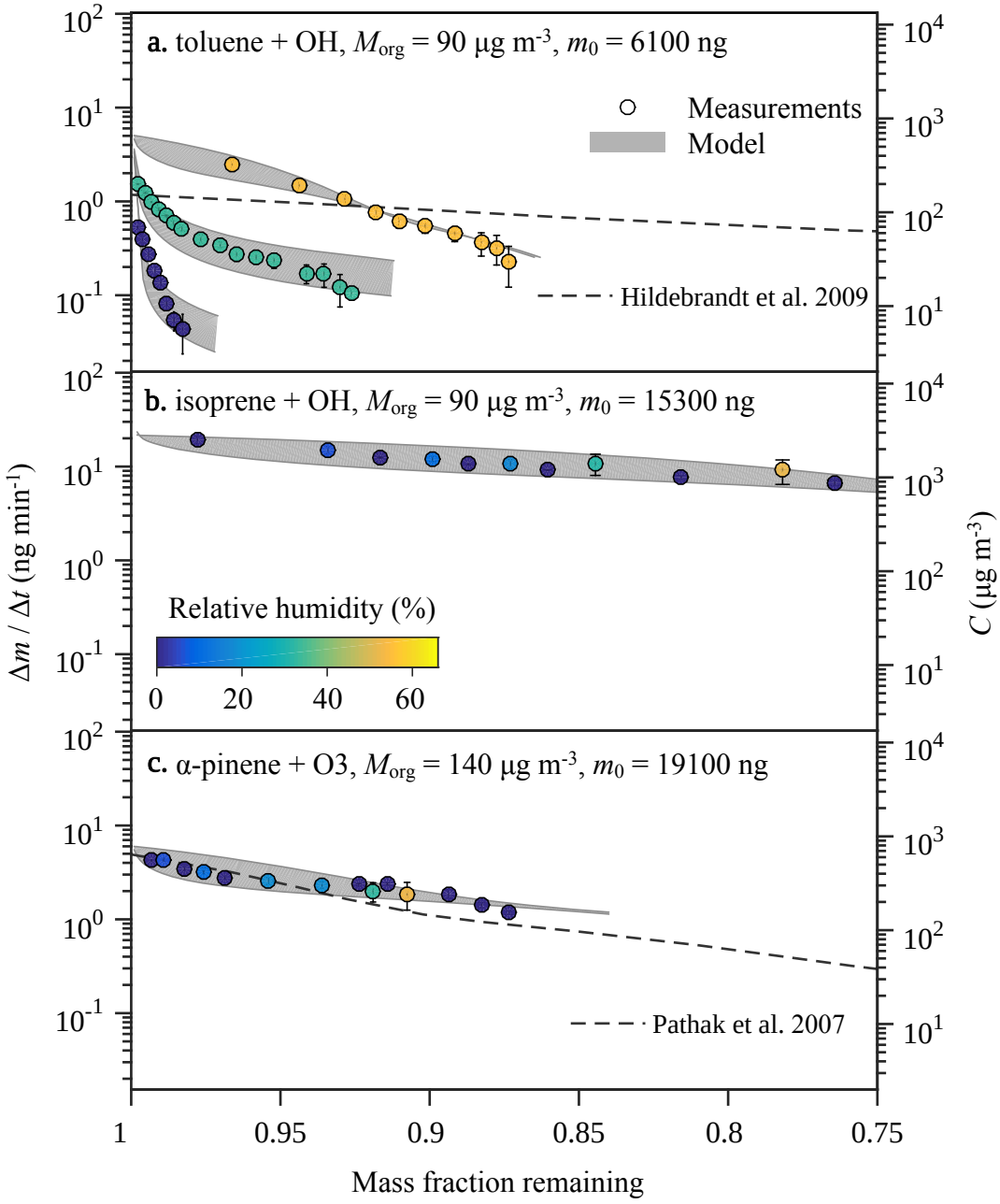
a. toluene + OH, M_{org} = 90 µg m^{-3}, m_0 = 6100 ng
Measurements
Model
Hildebrandt et al. 2009
b. isoprene + OH, M_{org} = 90 µg m^{-3}, m_0 = 15300 ng
Relative humidity (%)
0
20
40
60
c. α-pinene + O3, M_{org} = 140 µg m^{-3}, m_0 = 19100 ng
Pathak et al. 2007
Δm / Δt (ng min^{-1})
C (µg m^{-3})
Mass fraction remaining
1
0.95
0.9
0.85
0.8
0.75

Figure S2

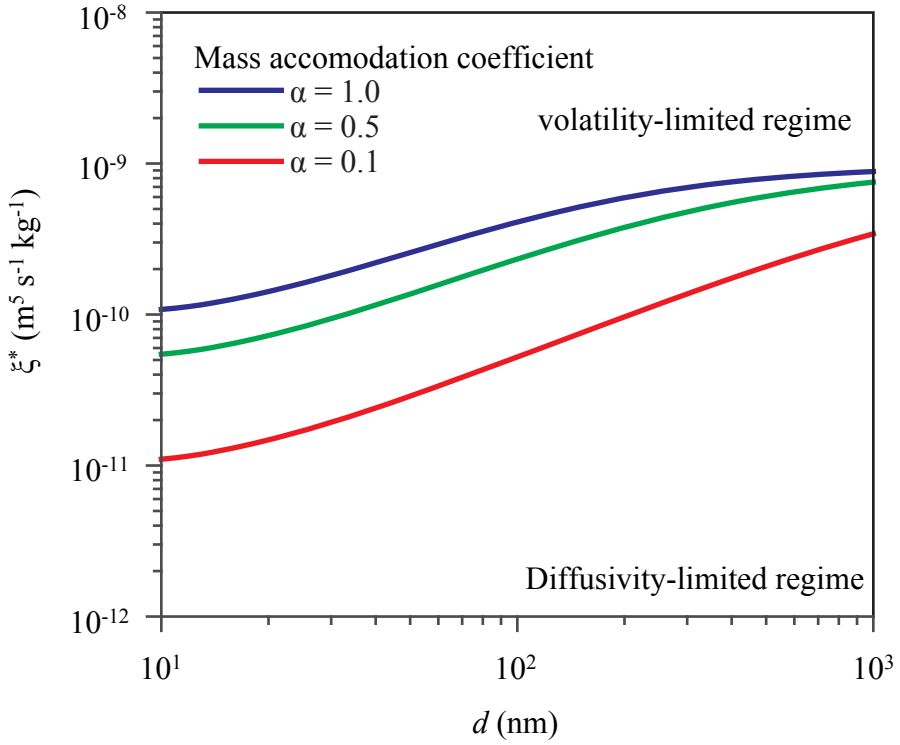
Mass accomodation coefficient
α = 1.0
α = 0.5
α = 0.1
volatility-limited regime
Diffusivity-limited regime
10-8
10-9
10-10
10-11
10-12
ξ* (m5 s-1 kg-1)
101
102
103
d (nm)

Figure S3

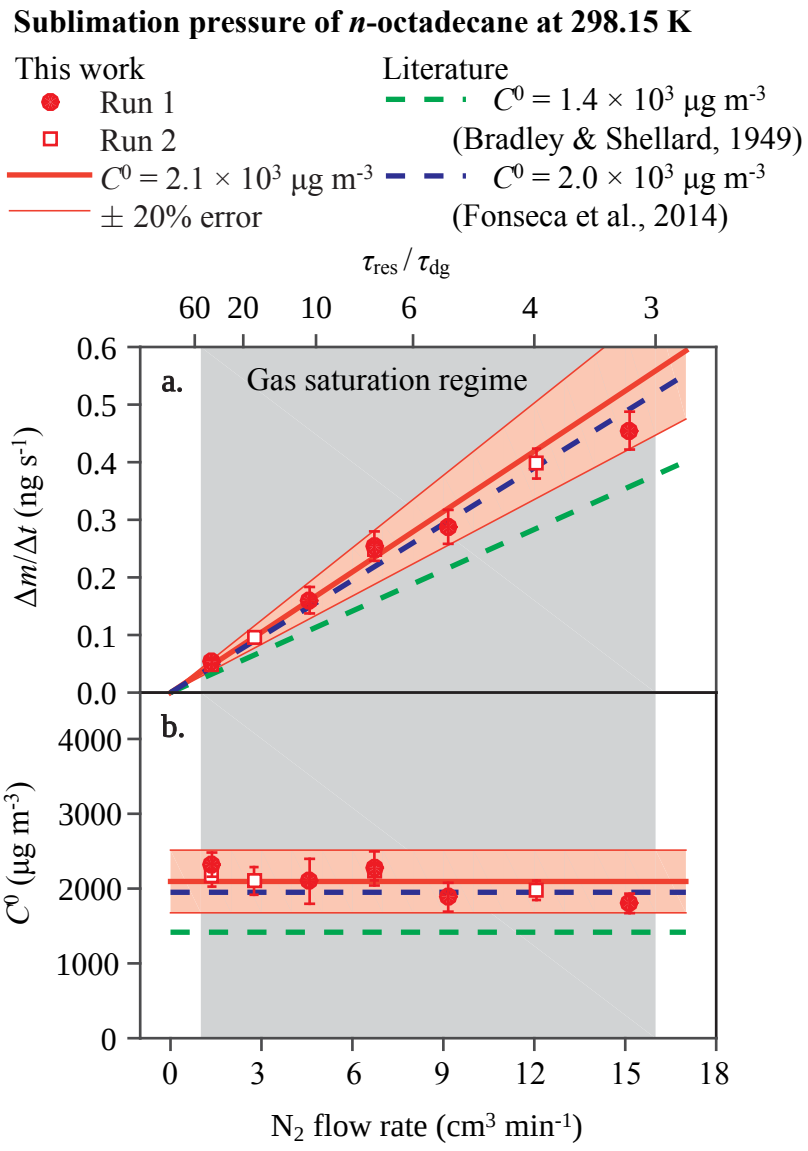
Sublimation pressure of n-octadecane at 298.15 K
This work
Run 1
Run 2
C⁰ = 2.1 × 10³ µg m⁻³
± 20% error
Literature
C⁰ = 1.4 × 10³ µg m⁻³
(Bradley & Shellard, 1949)
C⁰ = 2.0 × 10³ µg m⁻³
(Fonseca et al., 2014)
τres / τdg
60 20 10 6 4 3
a.
Gas saturation regime
Δm/Δt (ng s⁻¹)
0.6 0.5 0.4 0.3 0.2 0.1 0.0
b.
C⁰ (µg m⁻³)
4000 3000 2000 1000 0
0 3 6 9 12 15 18
N2 flow rate (cm³ min⁻¹)

Figure S4

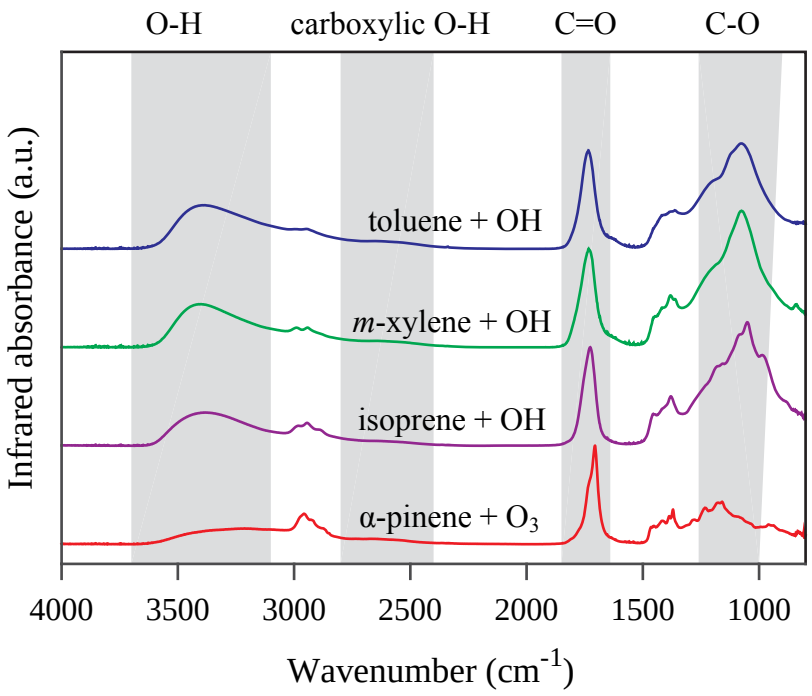
O-H
carboxylic O-H
C=O
C-O
Infrared absorbance (a.u.)
toluene + OH
m-xylene + OH
isoprene + OH
α-pinene + O3
4000
3500
3000
2500
2000
1500
1000
Wavenumber (cm-1)

Figure S5

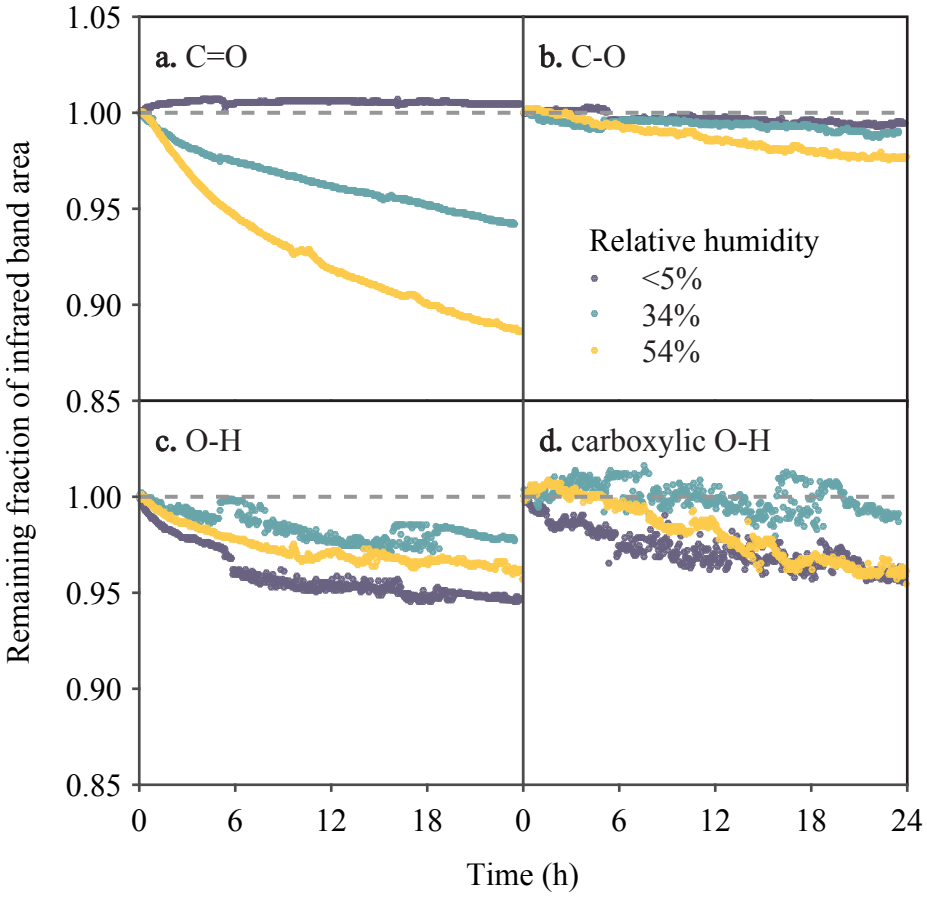
a. C=O
b. C-O
c. O-H
d. carboxylic O-H
Relative humidity
<5%
34%
54%
Remaining fraction of infrared band area
Time (h)
1.05
1.00
0.95
0.90
0.85
0
6
12
18
24

Figure S6

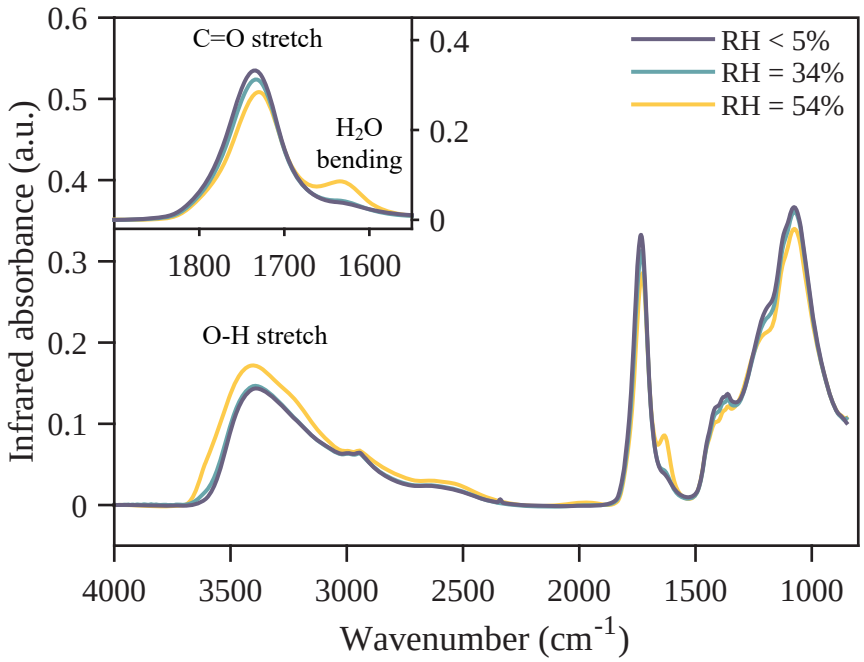
C=O stretch
H2O
bending
O-H stretch
RH < 5%
RH = 34%
RH = 54%
Infrared absorbance (a.u.)
Wavenumber (cm-1)
0.6
0.5
0.4
0.3
0.2
0.1
0
4000
3500
3000
2500
2000
1500
1000
1800
1700
1600
0.4
0.2
0

Figure S7